



# A smooth particle dynamics method considering material point failure for crack propagation simulation applied in rock mechanics

Yiwei Gao<sup>1</sup> · Xuhua Ren<sup>1</sup> · Jixun Zhang<sup>1</sup> · Tao Xu<sup>2</sup> · Hongyan Gu<sup>2</sup> · Xun Xiang<sup>1</sup> · Zhenyang Xin<sup>3</sup>

Received: 22 June 2022 / Accepted: 14 May 2023 / Published online: 29 September 2023  
© The Author(s), under exclusive licence to Springer Nature B.V. 2023

## Abstract

Numerical simulation of rock fracture mechanics has been a major research interest and challenging area in the field of rock mechanics. Based on this background, a smooth particle dynamics numerical simulation method (RGIMP) is proposed to consider the failed material point. The RGIMP algorithm is simple in form, does not need to use multiple velocity fields, takes advantage of the stability of the GIMP itself, and simulates the brittle fracture process of the rock by the failure process of the material point, and the resulting cracks are displayed. The accuracy of the RGIMP algorithm was verified via uniaxial compressive numerical simulations of a single-cleft standard cube specimen, a double-cleft standard cube specimen, and a double-cleft Brazilian disk specimen. Our research results provide a reference for the application of smooth particle dynamics methods in rock mechanics engineering and an understanding of rock fracture mechanisms.

**Keywords** RGIMP · Crack extension · Fracture mechanics · Numerical simulation

## 1 Introduction

Rocks are a typical anisotropic material (Zhao et al. 2022; Kou et al. 2021); there have various fine structural defects such as joints, cracks, pores, and faults occur within the rock. Under the action of the environment or external load, cracks sprout and expand at the defects, causing the rock structure to show a typical nonhomogeneous and nonlinear characteristic and irreversible damage to the rock. In recent years, research to reasonably

---

✉ Xuhua Ren  
renxh@hhu.edu.cn

Yiwei Gao  
gaoyiweijn@163.com

<sup>1</sup> College of Water Conservancy and Hydropower Engineering, Hohai University, Nanjing 210098, China

<sup>2</sup> Power China Chengdu Engineering Corporation Limited, Chengdu 610072, China

<sup>3</sup> School of Electrical and Mechanical Engineering, Xuchang University, Xuchang 461000, China

describe the variation pattern of nonlinear mechanical properties of rocks is popular and complicated.

Due to the diversity of rock cracks and the complexity of the extension process, as well as the difficult progress of theoretical analysis, experimental methods also encounter many challenges. With the rapid development of computer technology, numerical simulation methods have made great progress in recent years (Zhang et al. 2020; Yu et al. 2021), providing a better alternative for the study of the nonlinear characteristics of rocks. Compared with experimental studies, the cost of numerical simulation is low, and the whole process of dynamic fracturing of rocks can be predicted by providing reasonable constitutive relationships and computational parameters. Therefore, the nonlinear numerical simulation of rock has become increasingly popular among scholars.

The finite element method is one of the earliest numerical studies in rock fracture mechanics. Due to the large uncertainty in the crack extension direction (Yang et al. 2018), the finite element method needs to change the mesh generation of the crack tip at all times. Based on the finite element method, many crack treatment methods have been developed, such as the cohesive element method (Huang et al. 2022) and embedded discontinuous method (Lu et al. 2016), which can embed cracks into the mesh for treatment; however, there are some difficulties in dealing with the crack extension. Since the conventional finite element method cannot describe the discontinuous surfaces within the cell, the crack can only expand along the cell boundary or a given path, thus limiting the arbitrariness of the crack expansion direction. The extended finite element method (XFEM) can effectively solve the above problem (Rezan-zhad et al. 2019) and uses enrichment functions to describe the geometry of cracks; however, XFEM is developed from the finite element method and still has many difficulties in dealing with large deformations. The discrete element method (DEM) is another numerical simulation method after the finite element method (Gutiérrez-Ch et al. 2022) and simulates the whole process of crack expansion by establishing different contact models, and the most representative commercial software such as PFC3D has a wide range of applications in rock engineering (Khazaei et al. 2015; Bock and Prusek 2015). However, DEM requires parameter calibration to establish the relationship between macroscopic and fine-scale parameters (Zhou et al. 2015; Vahab et al. 2017), and DEM is not very advantageous in simulating continuous media.

Meshless methods are used to construct approximate functions without using meshes and have a wide range of applications in impact (Das and Eldho 2022), penetration, and explosion problems. Since cracks can expand in any direction without restriction in the meshless method, several meshless methods have been applied in the analysis and study of the dynamic fracture of rocks. The material point method (MPM) is a proposed meshless numerical method (Sulsky et al. 1994; Kan et al. 2021). In the MPM framework, the body is discretized into a set of material points (material points), and the body information (mass, velocity, etc.) is carried by the material points. In each computational step, the material points map the information into the background grid, which is used to compute the momentum equations. In solving the momentum equations, the material points are completely fixed to the background grid and move together with the background grid; after, the results of the background grid solution are mapped back to the material points to update their physical quantities. At the end of each computational step, the old background grid is discarded, and a new set of background grids is redrawn in the next computational step, thus avoiding problems such as large mesh deformations in the finite element method (Vaucorbeil et al. 2022). In the past 20 years, the MPM has been developed and successfully applied in the research fields of hypervelocity impact (Signetti and Heine 2021), explosion (Cui et al. 2014), fragmentation (Yang et al. 2012), and multiphase flow (Zhang et al. 2008). There is a disadvantage when using the MPM algorithm; when the material points cross the background grid, it produces a certain

perturbation, resulting in a reduction in calculation accuracy and even distortion of the calculation results. Based on this, Bardenhagen and Kober (2004) first proposed the generalized interpolation material point method (GIMP), which effectively suppresses the numerical noise due to material points crossing the background grid, and the GIMP algorithm obtains more accurate computational results than the MPM algorithm.

MPM was initially applied to the simulation of fracture mechanics. For example, multiple velocity fields are used to describe cracks (Nairn 2003); Nairn (2003) proposed the use of three velocity fields to model cracks. Although the three velocity fields are defined, each material point has at most two velocity fields, which is more problematic to implement because of the use of multiple velocity fields. (Wang et al. 2005) used irregular meshes to model two-dimensional cracks, using damaged material points to determine the approximate location of the cracks, but this method did not introduce explicit cracks.

In this paper, based on previous research, we propose an extremely simple numerical treatment of rock fracture, the generalized interpolation material point method in rock (abbreviated as RGIMP), relying on the more accurate calculation of the GIMP algorithm. The method is simple in form, does not need to use multiple velocity fields, and simulates the crack extension process by the failure process of the material point, and the resulting cracks are displayed. The damage criterion is used as a common Mohr–Coulomb criterion in rock mechanics, which simulates the progressive damage process of rocks by failing the material points when they reach a certain damage condition. This method has shown good performance in numerical tests, such as the maximum principal stress field distribution and crack expansion process. The results of the study provide a reference for the application of the GIMP method in the numerical simulation of rock fracture mechanics and an understanding of the mechanism of fracture extension and fracture interaction.

## 2 Fundamentals of the material point method

The material point method uses a dual description of Lagrangian particles and the Euler grid to discretize the continuum into a set of material points (Zhang et al. 2017), each of which represents a material region and carries all the information of this material region, such as stress, velocity, and mass. All material points carry all of the information of the continuum. In each calculation step, a new set of background grids is used, and the material points are solidly connected to the background grid and solved on the background grid using the standard finite element method; after, the grid node information is mapped back to the material points, and the deformed background grid is discarded at the end of each calculation step, thus avoiding difficulties in the numerical solution due to mesh distortion in the Lagrangian method. The material point method has higher computational efficiency and stability than smoothed particle hydrodynamics (SPH) (Zhang et al. 2017). Therefore, compared with SPH, the material point method can use more material points for calculation, and the results obtained are more accurate.

### 2.1 Control equation

In material region  $\Omega$ , the Lagrangian mass conservation equation is shown in the following equation:

$$\rho(X, t)J(X, t) = \rho_0(X) \quad (1)$$

$$\sigma_{ij,j} + \rho b_i - \rho \ddot{u}_i = 0 \quad (2)$$

The boundary condition is given by the following equation:

$$\sigma_{ij} n_j = \bar{t}_i \rightarrow \Gamma_t \quad (3)$$

$$u_i = \bar{u}_i \rightarrow \Gamma_u \quad (4)$$

where  $\rho$  is the density at the current moment,  $X$  denotes Lagrangian coordinates,  $t$  denotes the current time,  $J$  is the determinant of the deformation gradient,  $\sigma_{ij}$  denotes the Cauchy stress, and  $b_i$  is the force per unit material point acting on the object.  $\ddot{u}_i$  is the acceleration, and the subscripts  $i$  and  $j$  denote the components of the spatial variables, following the Einstein summation convention.  $n_j$  is the outer normal unit vector of the boundary, and  $u_i$  denotes the displacement.  $\Gamma_t$  and  $\Gamma_u$  are the given surface force boundary and the given displacement boundary of the material region  $\Omega$ , respectively.

The equivalent weak integral form of the momentum equation and the given surface force boundary conditions are given as follows:

$$\int_{\Omega} \rho \ddot{u}_i \delta u_i d\Omega + \int_{\Omega} \sigma_{ij} \delta u_{i,j} d\Omega - \int_{\Omega} \rho b_i \delta u_i d\Omega - \int_{\Gamma} \bar{t}_i \delta u_i d\Gamma = 0 \quad (5)$$

## 2.2 MPM foundation

In the MPM, the material region  $\Omega$  is discretized into a set of material points (Fig. 1a, b). Background grids are used to compute spatial derivatives and solve the momentum equation (Fig. 1c). The background grid is only solidly connected to material points at each time step, the deformed grid is discarded at the end of the time step, and a new background grid is generated for the next time step.

The displacement of the material point  $u_{ip}$  can be obtained by interpolating the background grid node displacement  $u_{il}$ , as shown in Eq. (6):

$$u_{ip} = N_{Ip} u_{il} \quad (6)$$

where  $N_{Ip}$  denotes the form function of the background grid node  $I$  at the material point  $p$ , in which the subscript  $p$  is associated with the material point  $p$  and the subscript  $I$  denotes the variable associated with the grid node  $I$ ; Eq. (6) follows the Einstein summation convention.

Using the material point as an integral point in equivalent weak integral form and applying the arbitrariness of the imaginary displacement, Eq. (7) can be obtained as follows:

$$\dot{p}_{il} = m_I \ddot{u}_{il} = f_{il}^{\text{int}} + f_{il}^{\text{ext}} \quad (7)$$

The momentum of the background grid node  $p_{il}$  is calculated as follows:

$$p_{il} = m_I v_{il} \quad (8)$$

The mass of the background grid node  $m_I$  is calculated as follows:

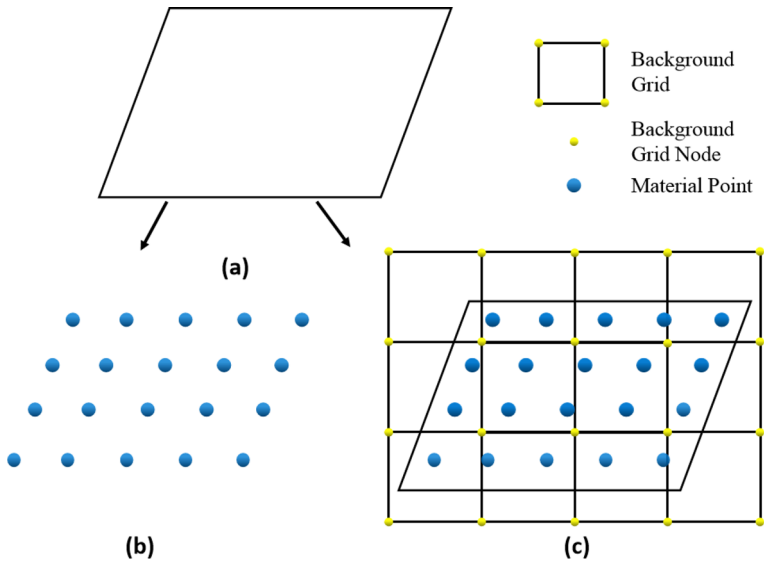


**Fig. 1** Schematic diagram of the MPM **a** material region; **b** the material region is discretized into material points; **c** background grid overlay material points

$$m_I = \sum_{p=1}^{n_p} N_{Ip} m_p \tag{9}$$

The internal force of the background grid node  $f_{il}^{int}$  is calculated as follows:

$$f_{il}^{int} = - \sum_{p=1}^{n_p} \frac{m_p}{\rho_p} N_{Ip,j} \sigma_{ijp} \tag{10}$$

The internal force of the background grid node  $f_{il}^{ext}$  is calculated as follows:

$$f_{il}^{ext} = \sum_{p=1}^{n_p} m_p N_{Ip} b_{ip} \tag{11}$$

### 2.3 GIMP foundation

In the MPM algorithm, numerical noise is generated when the material points cross the background grid, which affects the calculation accuracy. To reduce the numerical noise generated by material points crossing the background grid boundary, the GIMP algorithm was first proposed by Bardenhagen and Kober (2004). In the GIMP algorithm, the material domain is discretized into material points represented by characteristic functions with a certain size.

The GIMP algorithm considers the effect of the support domain of the material point, and the support domain of a material point represents the area occupied by the material point in the simulation object. When the number of material points is greater, the support domain of each material point will be smaller, and the calculation result is more accurate.

The characteristic function of the material point is  $\chi_p(x)$ , and the approximation of the physical quantity  $f$  is shown in Eq. (12):

$$f(x) = \sum_p f_p \chi_p(x) \quad (12)$$

where  $f_p$  is the value of the physical quantity at material point  $p$ .

The trial function of GIMP is the eigenfunction  $\chi_p(x)$ , and the test function is the background grid shape function  $N_i(x)$ . Then, the shape function  $N_{ip}$  in MPM is replaced by  $S_{ip}$ , as shown in Eq. (13):

$$S_{ip} = \frac{1}{V_p} \int_{\Omega_p \cap \Omega} \chi_p(x) N_i(x) d\Omega \quad (13)$$

where  $V_p$  is the volume of the material point, calculated as in Eq. (14):

$$V_p = \int_{\Omega_p \cap \Omega} \chi_p(x) dV \quad (14)$$

The form function  $S_i$  of GIMP is smoother and has a larger support domain compared to the form function  $N_i$  of MPM.

When GIMP satisfies Eq. (15), its characteristic functions degenerate to those of MPM, as follows:

$$\chi_p(x) = \delta(x - x_p) dV \quad (15)$$

The background grid shape function  $N_i(x)$  of GIMP is generally linear, and the one-dimensional case is shown in Eq. (16):

$$N_i(x) = \begin{cases} 0 & |x - x_i| \geq L \\ 1 + (x - x_i)/L & -L < x - x_i \leq 0 \\ 1 - (x - x_i)/L & 0 < x - x_i < L \end{cases} \quad (16)$$

In Eq. (16),  $L$  is the length of the background grid, and the feature function  $\chi_p(x)$  takes the simplest form, as shown in Eq. (17):

$$\chi_p(x) = \begin{cases} 1 & x \in \Omega_p \\ 0 & x \notin \Omega_p \end{cases} \quad (17)$$

Therefore, the expression of the form function of the GIMP can be obtained as shown in Eq. (18):

$$S_{ip} = \begin{cases} 0 & |x_p - x_i| \geq L + l_p \\ \frac{(L+l_p+(x_p-x_i))^2}{4Ll_p} & -L - l_p < x_p - x_i \leq -L + l_p \\ 1 + \frac{x_p-x_i}{L} & -L + l_p < x_p - x_i \leq -l_p \\ 1 - \frac{(x_p-x_i)^2+l_p^2}{2Ll_p} & -l_p < x_p - x_i \leq l_p \\ 1 - \frac{x_p-x_i}{L} & l_p < x_p - x_i \leq L - l_p \\ \frac{(L+l_p-(x_p-x_i))^2}{4Ll_p} & L - l_p < x_p - x_i \leq L + l_p \end{cases} \tag{18}$$

where  $2l_p$  is the characteristic length of the material point  $p$ .

$S_{ip}$  has the continuity of  $C^1$ , and its shape is compared with the shape function of MPM, as shown in Fig. 2.

In the three-dimensional space,  $S_{ip}$  is shown in Eq. (19):

$$S_{ip}(x) = S_{ip}(\xi)S_{ip}(\eta)S_{ip}(\zeta) \tag{19}$$

where  $\xi=|(x_p - x_i)/L|$ ,  $\eta=|(y_p - y_i)/L|$ ,  $\zeta=|(z_p - z_i)/L|$ .

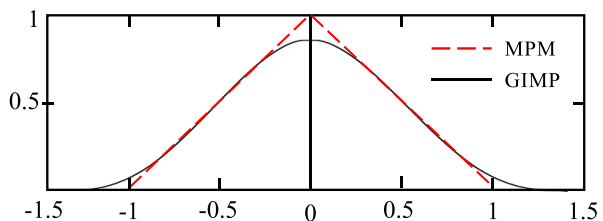
### 3 Fracture treatment of RGIMP

#### 3.1 Fracture criterion

RGIMP is a proposed numerical simulation method of rock fracture based on the GIMP algorithm. The damage and destruction of materials are an unavoidable and a very difficult problem. Due to different material properties and different modes of loading action, the damage modes and failure states of materials are different, and appropriate damage failure models need to be used according to specific problems. After the damage failure of the material, its load-bearing capacity is reduced or even unable to carry. In the GIMP algorithm, the physical quantity of the material is carried by the material point; therefore, the damage failure of the material also needs to be reflected by the failure of the material point.

In the material point method, the common damage failure methods are divided into the following categories: maximum equivalent plastic strain failure model, maximum hydrostatic tension failure model, maximum principal stress/shear stress failure model, and maximum principal strain/shear strain failure model. For example, the maximum equivalent plastic strain failure model requires specifying the equivalent plastic strain  $\epsilon_{fail}$  when the material point fails. When the equivalent plastic strain  $\epsilon^p$  of the material point is greater

Fig. 2 Comparison of shape functions of MPM and GIMP



than  $\varepsilon_{\text{fail}}$ , the material point is determined to have failed. In this case, it is necessary to develop a failure process for the failed material point.

In rock mechanics, the Mohr–Coulomb criterion is one of the more commonly used damage criteria, is widely recognized by numerous scholars, and has been widely used in previous numerical simulations of fracture mechanics and achieved better results. In this paper, the Mohr–Coulomb criterion is selected as the fracture criterion, and the expressions of the Mohr–Coulomb criterion are shown in Eqs. (20) and (21):

$$\sigma_f = \sigma_t \quad (20)$$

$$\tau_f = c + \sigma_f \tan \phi \quad (21)$$

where  $\sigma_f$  and  $\tau_f$  are the maximum tensile and shear stresses at the hypothetical damage surface, respectively,  $\sigma_t$  is the tensile strength of the material,  $c$  is the cohesive force of the material, and  $\phi$  is the angle of internal friction of the material. When the material point satisfies the tensile damage condition (i.e., Eq. 20), the tensile damage is determined as a priority, and when Eq. (20) is not satisfied, then, the shear damage is determined (i.e., Eq. 21).

### 3.2 Failure treatment of material point

In the material point method, the failure of the material point is treated in a relatively simple way, which is very helpful for the treatment of mechanical problems in engineering. When the material point is determined to fail, the bias stress of the failed material point is set to zero, while no further correction is made for the sound velocity and pressure of its artificial volume viscosity. Currently, the following treatments for the pressure of the failed material point are available (Zhang et al. 2017):

1. The material point cannot withstand the tensile force after failure but can withstand the pressure.
2. The material point can withstand neither pressure nor tension after failure.
3. The material point can withstand a certain tensile force after failure but can also withstand a certain pressure, and the pressure threshold range needs to be set.
4. In this paper, we mainly simulate the mechanical behavior of the rock under pressure; thus, the first pressure treatment is selected; the material point cannot withstand the tensile force after failure but can withstand the pressure.

When the material point fails, the color of the failed material point is displayed; thus, the resulting cracks are displayed. As shown in Fig. 3, the blue material points are unfailed material points, and the red material points are failed material points.

When there is no failure of material points, the blue dots represent rocks, and the yellow area represents the initial crack, as shown in Fig. 3a. As the experiment progresses, stress concentration automatically occurs at the tip of the initial crack. The material points are determined using Eqs. (20) and (21), and when a material point reaches the failure criterion, the bias stress of the failed material point is set to a constant value of 0. The failed material points are shown as red dots in Fig. 3b. By setting the bias stress to 0, the effect of the material point can be basically disregarded, and the material point with a bias stress of 0 is similar to the crack generated in the physical experiments. In the subsequent calculation, the failed material points are similar to the cracks or gaps generated in the physical



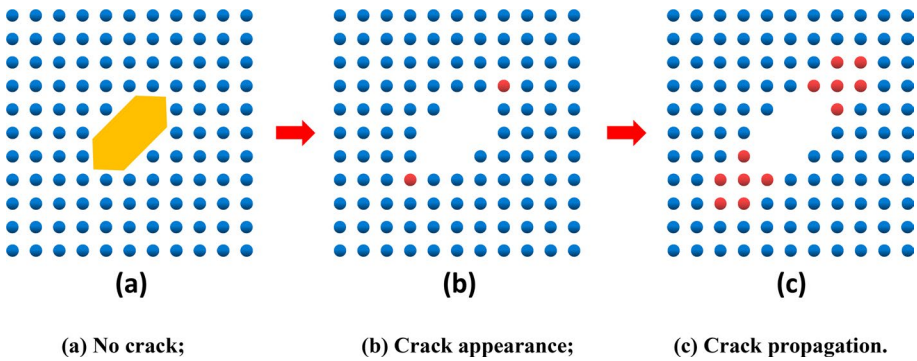


**Fig. 3** Display processing of the failed material point **a** no crack; **b** crack appearance; **c** crack propagation

experiments. The material point that has just failed is the crack tip, and the crack propagates automatically along the crack tip, as shown in Fig. 3c. Throughout the calculation process, there is no need to identify the crack tip. Therefore, the simulation of cracks in the material point method is relatively simple.

### 3.3 Time step

To ensure the stability of the numerical calculation, the time step length needs to be smaller than the critical time step length. Specifically, within one time step, the propagation distance of any information cannot exceed the size of a background grid. Since a constant background grid is used in the calculation, the time step is also a constant value. The formula for the critical time step  $\Delta t_{cr}$  is shown as Eq. (22) (Zhang et al. 2017):

$$\Delta t_{cr} = \min \frac{l_e}{p \ c + |v|} \tag{22}$$

In Eq. (22),  $l_e$ ,  $p$ ,  $|v|$  and  $c$  denote the size of the background grid, the material point, the maximum absolute velocity of the material point, the current material speed of sound, respectively.  $c$  is calculated as shown in Eq. (23):

$$c = \sqrt{E(1 - \mu)/[(1 + \mu)(1 - 2\mu)\rho]} \tag{23}$$

In Eq. (23),  $E$ ,  $\mu$  and  $\rho$  denote the modulus of elasticity, Poisson’s ratio, and density of the material point, respectively. In practical problems,  $c$  is generally an unknown variable; thus, it is difficult to obtain a constant time step  $\Delta t$ . Equation (24) is generally used to calculate the constant time step:

$$\Delta t = \alpha \min \frac{l_e}{p \ c} \tag{24}$$

In Eq. (24),  $\alpha$  is the time step factor and uses values from 0 to 1.

The time step factor  $\alpha$  is taken as 0.1 because the maximum absolute velocity  $|v|$  of the material point is low in our study. The time steps  $\Delta t$  are all smaller than the critical time step  $\Delta t_{cr}$ , ensuring the stability of the calculation.

## 4 Numerical algorithm verification

To verify the accuracy of the RGIMP numerical simulation method, numerical simulations were conducted for three numerical cases, and the calculated results were compared with the existing experimental results, numerical simulation results, and theoretical calculation results for verification. The first example is the simulation of the fracture expansion process of a standard cube specimen with a single inclined fracture under uniaxial compression, the second example is the simulation of the fracture expansion process of a standard cube specimen with a double inclined fracture under uniaxial compression, and the third example is the simulation of the fracture expansion process of a Brazilian disk specimen with double fracture under uniaxial compression. The above calculation example is used to illustrate the applicability of the RGIMP algorithm in the numerical simulation of rock fractures. The main purpose of the algorithm is to show the progressive damage process of cracks and the change trend of the crack morphology; therefore, the parameters of the model are not calibrated, and the elastic parameters of the model are set to be consistent, with a density  $\rho$  of 2600 kg/m<sup>3</sup>, elastic modulus  $E$  of 17 GPa, and Poisson's ratio  $\mu$  of 0.14.

### 4.1 Numerical simulation of compression and shear failure of a single crack specimen

The example sizes of the single fracture compression and shear numerical simulation specimens were obtained from the literature (Liu et al. 2020) and are shown in Fig. 4. Figure 4a shows the model size, and Fig. 4b shows the material point distribution of Example 1. The specimen is a standard cubic specimen with a length of 50 mm and a

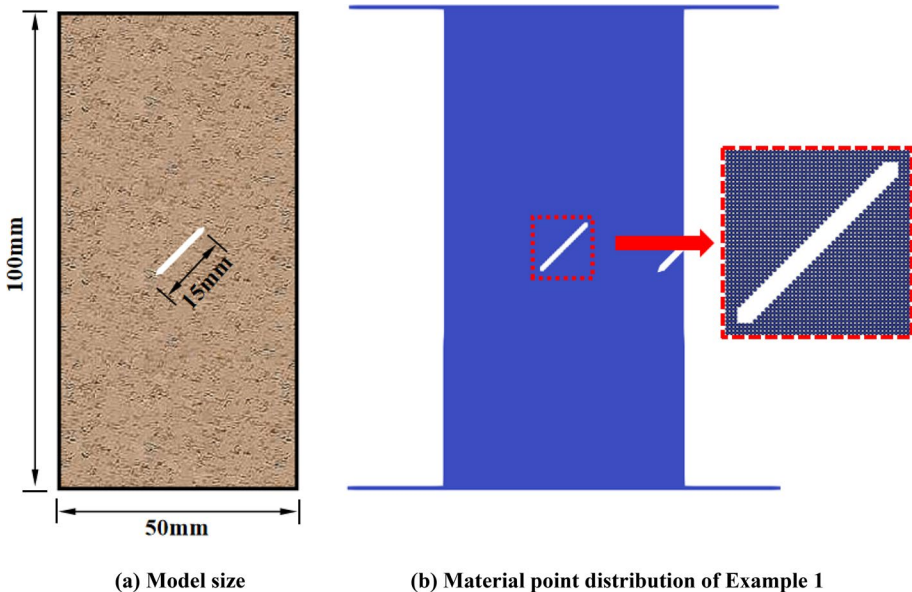


**Fig. 4** Model size and material point distribution of Example 1 **a** model size; **b** material point distribution of Example 1

height of 100 mm, with a prefabricated gap of 15 mm in the center of the specimen, and the angle between the gap and the horizontal direction is  $45^\circ$ . The specimen was discretized as 80,326 material points with a background grid length of 0.5 mm, and the model was loaded in displacement loading mode with a loading rate of  $5e-4$  mm/s in agreement with the literature (Liu et al. 2020). The cohesive force of the specimen is 5.95 MPa, the internal friction angle is  $40^\circ$ , and the tensile strength is 2 MPa.

The maximum principal stress cloud on the edge of the crack expansion is shown in Fig. 5. Figure 5a shows the calculation result of the RGIMP algorithm, and Fig. 5b shows the calculation result of Abaqus finite element software. The calculation result of Abaqus only compares the shape of the cloud map with the calculation result of the RGIMP algorithm, and the same is true for Example 2 and Example 3. As seen in Fig. 5a, the maximum value of the principal stress is concentrated at the crack tip, predicting that the crack will start to expand at the crack tip, and the same calculation result is obtained by Abaqus. The maximum principal stress cloud calculated by the RGIMP algorithm is in general agreement with the result of Abaqus, which verifies the accuracy of the calculation result of the RGIMP algorithm in terms of the principal stress in rocks.

The asymptotic damage process of Example 1 is shown in Fig. 6, and the step indicates a time step. The “wing crack” arises from the tip of the precast crack and extends up and down in the loading direction. This crack extension morphology is in general agreement with that of the experimental result (DIC) (Fig. 7a) of the literature (Liu et al. 2020). Figures 7b and c shows the experimental result and theoretical calculation result of from the literature (Yang and Jing 2011), respectively. The calculation result of the RGIMP algorithm is consistent with the experimental and theoretical calculation results of the literature (Yang and Jing 2011), verifying the accuracy of the calculation result of the RGIMP algorithm in rock fracture. Figure 7d shows the numerical calculation result of the numerical flow form method in the literature (Yang et al. 2014), and

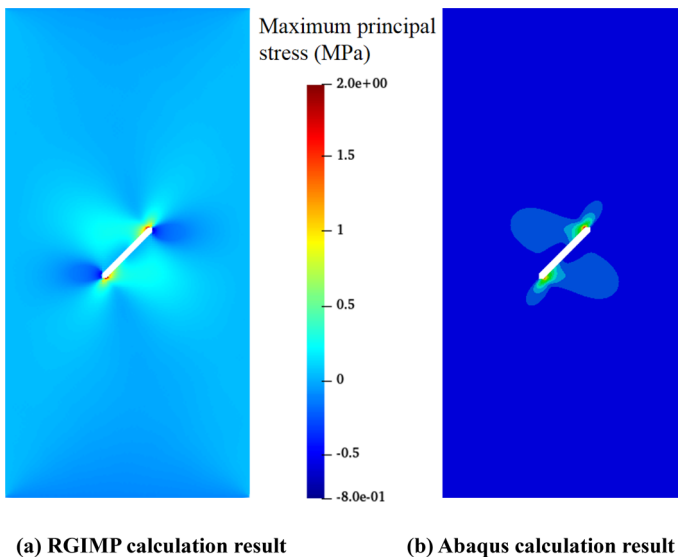


**Fig. 5** Maximum principal stress cloud for Example 1 **a** RGIMP calculation result; **b** Abaqus calculation result

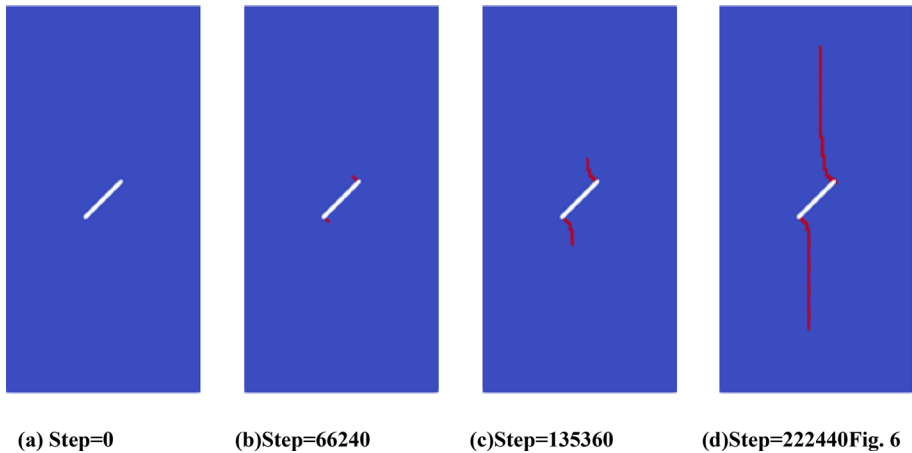


**Fig. 6** Crack extension process of Example 1 **a** Step=0, **b** Step=66,240, **c** Step=135,360, **d** Step=222,440

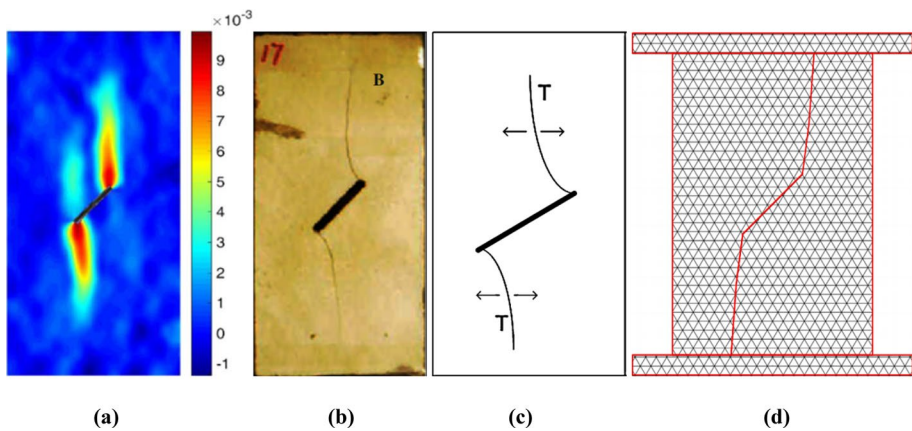


**Fig. 7** Crack extension of Example 1 and comparison with previous studies **a** DIC results from Liu et al. (2020), **b** Test results from Yang et al. (2011), **c** Theoretical model from Yang et al. (2011), **d** NMM results from Yang et al. (2014)

the RGIMP algorithm can better reflect the real crack extension pattern compared to the straight-up and straight-down cracks calculated in the literature (Yang et al. 2014).

#### 4.2 Numerical simulation of compression and shear failure of a double crack specimen

The dimensions of the numerical simulation example of compression shear for the double fracture were obtained from the literature (Lin et al. 2021) and are shown in Fig. 8. Figure 8a represents the model size, and Fig. 8b represents the material point distribution of Example 2. The specimen is a standard cubic specimen with a length of 70 mm and a height of 140 mm, with two cracks 15 mm in length prefabricated in the center of the

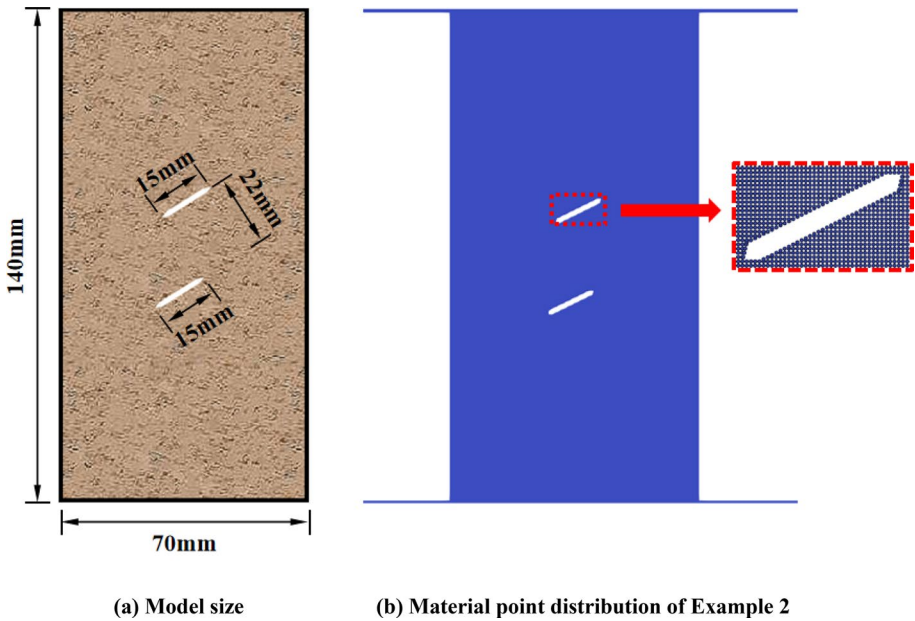


**Fig. 8** Model size and material point distribution of Example 2 **a** Model size, **b** Material point distribution of Example 2

specimen. The angle between the cracks and the horizontal direction is  $30^\circ$ , and the distance between the two cracks is 22 mm. The specimen was discretized into 79,976 material points with a background grid length of 0.7 mm, and the specimen was loaded in displacement loading mode with a loading rate of  $1e-2$  mm/s in agreement with the literature (Lin et al. 2021). The cohesive force of the specimen is 5.95 MPa, the internal friction angle is  $40^\circ$ , and the tensile strength is 2 MPa.

The maximum principal stress cloud on the edge of crack expansion is shown in Fig. 9. Figure 9a shows the calculation result of the RGIMP algorithm, and Fig. 9b shows the calculation result of Abaqus finite element software. As seen in Fig. 9, the maximum value of the principal stress calculated by the RGIMP algorithm is concentrated at the crack tip of the double cracks, indicating that the cracks will start to expand at the crack tip. The maximum principal stress cloud obtained by the RGIMP algorithm is consistent with the result of Abaqus, which verifies the accuracy of the calculation result of the RGIMP algorithm in terms of the maximum principal stress in rocks.

The asymptotic damage process of Example 2 is shown in Fig. 10, and the step indicates a time step. The “wing-shaped crack” emerges from the tip of the precast crack, the upper crack of the bottom crack and the lower crack of the top crack; these gradually approach each other and eventually merge, and the upper crack of the top crack and the lower crack of the bottom crack expand up and down along the loading direction until reaching the top and bottom of the specimen, respectively. The crack extension morphology is in general agreement with the crack extension morphology (Fig. 11a) of the test result (S-120-30) of the literature (Lin et al. 2021). Figure 11b shows the theoretical calculation result from the literature (Omer and Kareem 2004), and the result shows that the upper and lower fissures expand up and down along the loading direction, respectively, and the two fissures in the middle gradually come together and merge, which is consistent with the numerical

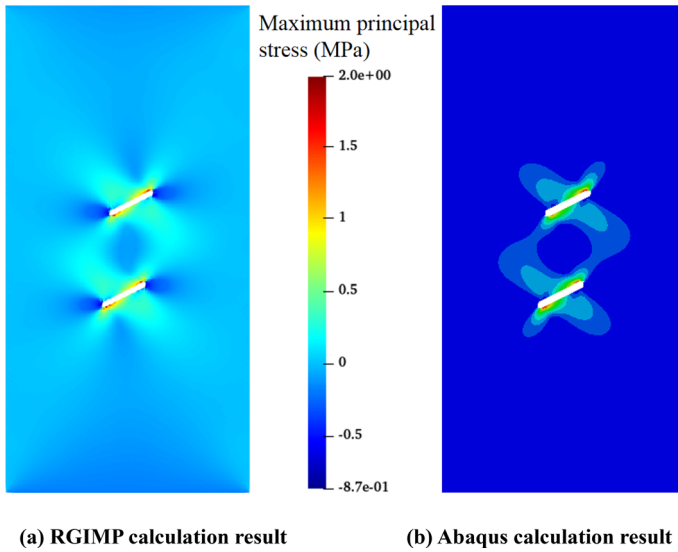


**Fig. 9** Maximum principal stress cloud for Example 2 **a** RGIMP calculation result, **b** Abaqus calculation result

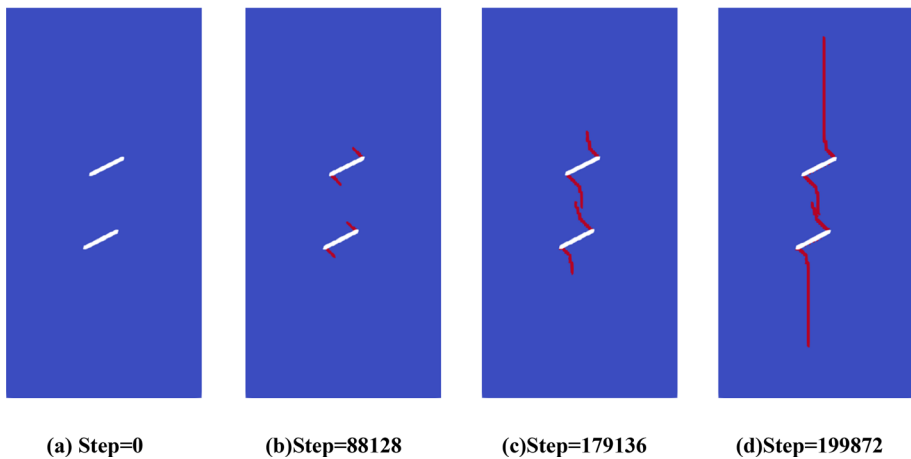
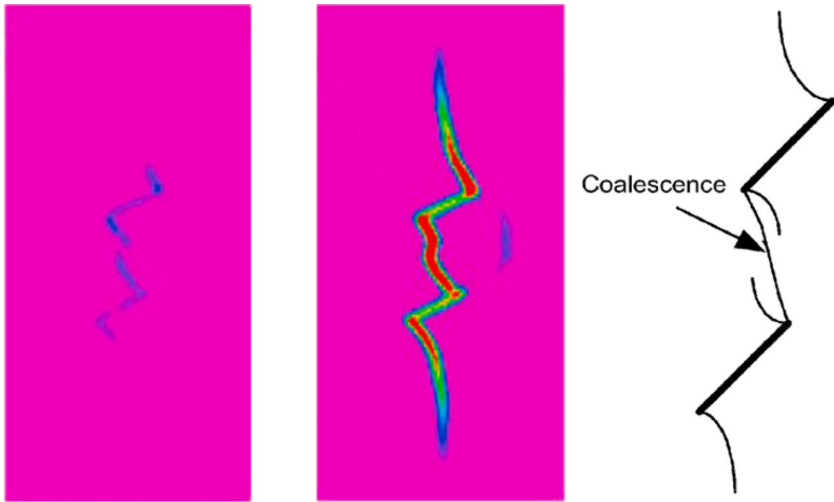


**Fig. 10** Crack extension process of Example 2 **a** Step=0, **b** Step=88,128, **c** Step=179,136, **d** Step=199,872

simulation result of the RGIMP algorithm. Example 2 verifies the accuracy of the RGIMP algorithm calculation results in terms of the process of rock crack expansion.

#### 4.3 Numerical simulation of compression and shear failure of double crack brazilian disk specimen

The dimensions of the arithmetic example for the Brazilian disk compression and shear numerical simulation specimen were obtained from the literature (Aliabadian et al.

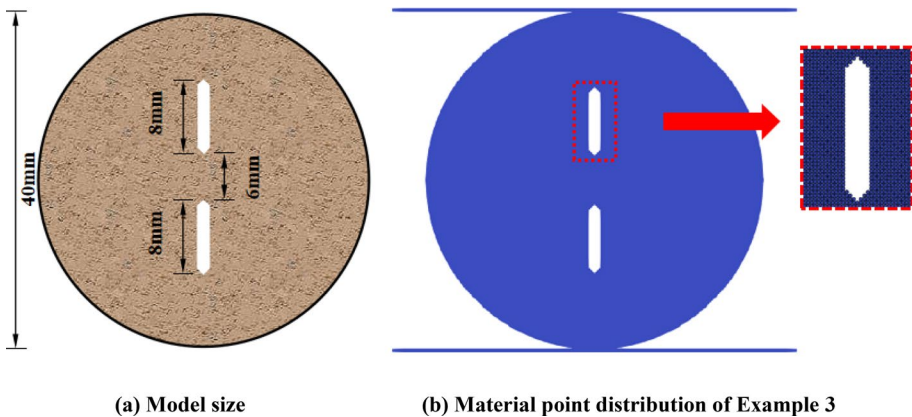


(a) Test results from (Lin et al. 2021) (b) Theoretical model from (Omer et al. 2004)

2004)

**Fig. 11** Crack extension of Example 2 and comparison with previous studies **a** test results from (Lin et al. 2021), **b** theoretical model from (Omer et al. 2004)

2021) and are shown in Fig. 12. Figure 12a shows the model size, and Fig. 12b shows the material point distribution of Example 3. The specimen is a Brazilian disk with a diameter of 40 mm, and the center of the specimen is prefabricated with 2 cracks of 8 mm in length. The angle between the cracks and the horizontal direction is 90°, and the spacing between the two cracks is 6 mm. The specimen was discretized as 31,672 material points with a background grid length of 0.5 mm, and the model was loaded in



(a) Model size

(b) Material point distribution of Example 3

**Fig. 12** Model size and material point distribution of Example 3 **a** model size, **b** material point distribution of Example 3



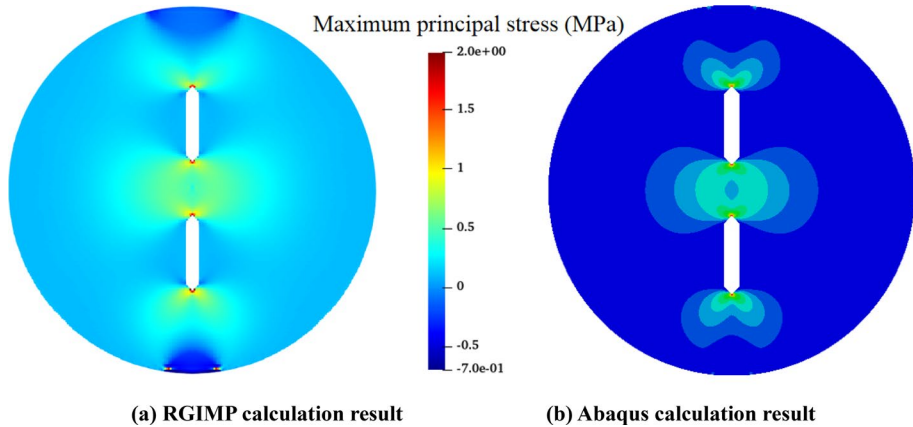


**Fig. 13** Maximum principal stress cloud for Example 3 **a** RGIMP calculation result, **b** Abaqus calculation result

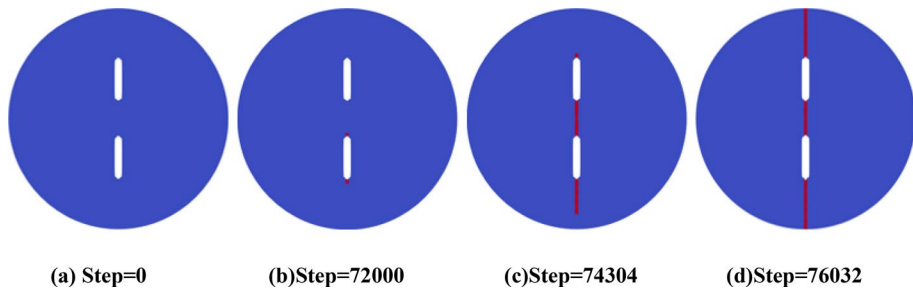


**Fig. 14** Crack extension process of Example 3 **a** Step=0, **b** Step=72,000, **c** Step=74,304, **d** Step=76,032

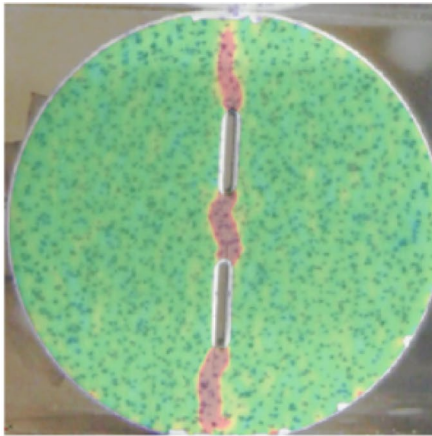
displacement loading mode with a loading rate consistent with the literature (Aliabadian et al. 2021) at  $4e-3$  mm/s. The cohesive force of the specimen is 5.95 MPa, the internal friction angle is  $40^\circ$ , and the tensile strength is 2 MPa.

The maximum principal stress cloud on the eve of crack expansion in the Brazilian disk is shown in Fig. 13. Figure 13a shows the calculation result of the RGIMP algorithm, and Fig. 13b shows the calculation result of Abaqus finite element software.

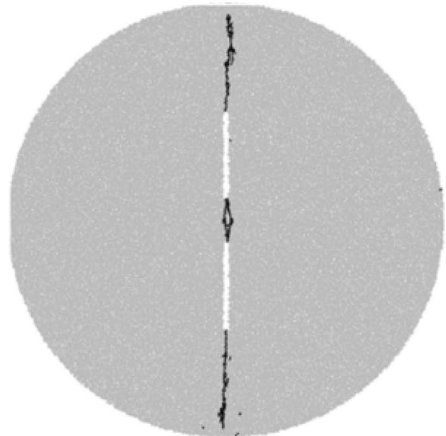
As seen in Fig. 13, the maximum principal stress cloud obtained by the RGIMP algorithm is consistent with the result of Abaqus. Once again, the accuracy of the calculation result of the RGIMP algorithm proposed in this paper in terms of the maximum principal stress in rocks is verified.

The crack expansion process of the Brazilian disk specimen is shown in Fig. 14, and the step indicates a time step. The cracks initially began at the top and bottom tips of the bottom crack and then, expanded up and down along the loading direction, respectively. Later, cracks were also generated at the top and bottom tips of the top crack, which first penetrated between the two cracks and then, extended to the bottom and top of the Brazilian disc.





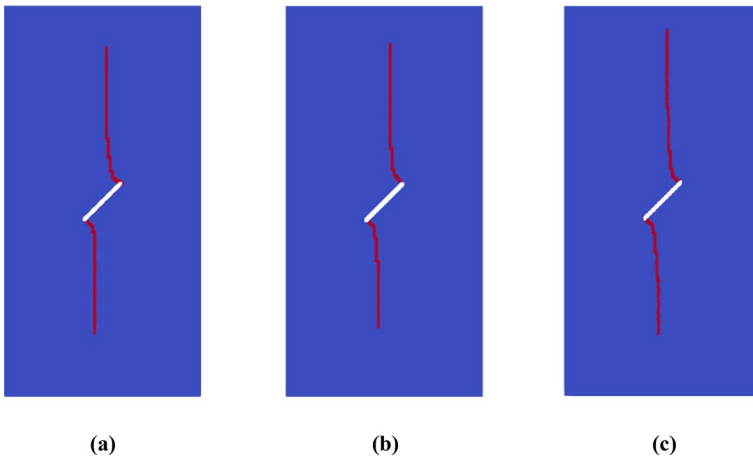
(a) DIC results from (Aliabadian et al. 2021)



(b) BEM results from (Aliabadian et al. 2021)

**Fig. 15** DIC result and BEM result from (Aliabadian et al. 2021) **a** DIC results from (Aliabadian et al. 2021), **b** BEM results from (Aliabadian et al. 2021)

Figure 15 shows the DIC calculation result (Fig. 15a) and BEM calculation result (Fig. 15b) in the literature (Aliabadian et al. 2021), and the numerical simulation result of the RGIMP algorithm is in basic agreement with the calculation result of the DIC and the simulation result of BEM, which further verifies the accuracy of the calculation result of the RGIMP algorithm in terms of rock crack extension.



(a)

(b)

(c)

**Fig. 16** Result verification of Example 1 **a** example 1; **b** material point reduction by 1/8; **c** material point reduction by 1/4

## 5 Discussion

In Sect. 4, the applicability of RGIMP in rock crack propagation was verified through three examples. In the finite element method, the calculation can be interrupted due to the mesh distortion, but this situation does not exist in the material point method. If the material point method uses an infinite number of calculation steps, then, it continues its calculations. During the calculation process, result files are continuously outputted. When reasonable results are obtained, the calculation can be manually stopped, so there is no non-convergence in the calculation of the material point method.

In the same calculation conditions, RGIMP has only one calculation result; therefore, its calculation result is relatively stable, which is similar to the finite element method. In the finite element method, a finer mesh division correlates to more accurate calculation results, and the same applies to the material point method. When there are more material points, the calculation results are more accurate. Figure 16 shows the calculation results of Example 1 (Fig. 16a) and the reduction in the total number of material points by 1/8 (Fig. 16b) and 1/4 (Fig. 16c). Their calculation results are basically the same, but more material points correlated with a more accurate simulation of the crack extension.

## 6 Conclusion

1. In this paper, a crack propagation simulation applied in rock mechanics (RGIMP) is proposed. RGIMP takes advantage of the stability of the GIMP algorithm itself to simulate the brittle fracture process of rocks by the failure process of material points. Compared with the previous numerical simulation of rock fracture by the MPM algorithm, the RGIMP algorithm is simpler and easier to implement and does not require the use of multiple velocity fields, and the resulting cracks are displayed.
2. Uniaxial compression tests on a single-cleft standard cube specimen, double-cleft standard cube specimen, and double-cleft Brazilian disk specimen were conducted to verify the accuracy of the RGIMP algorithm. Crack extension processes and the maximum principal stress clouds calculated by the RGIMP algorithm are highly similar to previous experimental results, numerical simulation results, and finite element calculation results.
3. At present, the RGIMP algorithm is only in its preliminary exploration stage, and this paper only verifies its applicability in rock fracture. Applicability of the RGIMP algorithm to other common geotechnical engineering problems, such as landslides, hydraulic splitting, tunnel collapse, and rock bursts, still needs to be explored and thoroughly refined.

**Author contributions** All authors contributed to the study's conception and design. Writing ideas were provided by XR and JZ. Data collection was performed by TX, HG, XX, ZX, and the first draft of the manuscript was written by YG. All authors commented on previous versions of the manuscript. All authors read and approved the final manuscript.

**Funding** This work was supported by the Postgraduate Research and Practice Innovation Program of Jiangsu Province (KYCX21\_0517), Science and Technology Special Program of Power China Chengdu Engineering Corporation Limited (821019716), Major Science and Technology Special Program of Yunnan Province (202102AF080001), and Fundamental Research Funds for the Central Universities (B220204001).

## Declarations

**Conflict of interest** The authors have no relevant financial or nonfinancial interests to disclose.

## References

- Aliabadian Z, Sharafisafa M, Tahmasebinia F, Shen LM (2021) Experimental and numerical investigations on crack development in 3D printed rock-like specimens with pre-existing flaws. *Eng Fract Mech* 241:107396. <https://doi.org/10.1016/j.engfracmech.2020.107396>
- Bardenhagen SG, Kober EM (2004) The generalized interpolation material point method. *Comp Model Eng Sci* 5(6):477–495. <https://doi.org/10.3970/CMES.2004.005.477>
- Bock S, Prusek S (2015) Numerical study of pressure on dams in a backfilled mining shaft based on PFC3D code. *Comput Geotech* 66:230–244. <https://doi.org/10.1016/j.compgeo.2015.02.005>
- Cui XX, Zhang X, Zhou X, Liu Y, Zhang F (2014) A Coupled finite difference material point method and its application in explosion simulation. *Comp Model Eng Sci* 98(6):565–599. <https://doi.org/10.3970/cmcs.2014.098.565>
- Das S, Eldho TI (2022) A meshless weak strong form method for the groundwater flow simulation in an unconfined aquifer. *Eng Anal Bound Elem* 137:147–159. <https://doi.org/10.1016/j.enganabound.2022.02.001>
- Gutiérrez-Ch JG, Senent S, Zeng P, Jimenez R (2022) DEM simulation of rock creep in tunnels using rate process theory. *Comput Geotech* 142:104559. <https://doi.org/10.1016/j.compgeo.2021.104559>
- Huang Y, Zolfaghari N, Bungler AP (2022) Cohesive element simulations capture size and confining stress dependence of rock fracture toughness obtained from burst experiments. *J Mech Phys Solids* 160:104799. <https://doi.org/10.1016/j.jmps.2022.104799>
- Kan L, Liang Y, Zhang X (2021) A critical assessment and contact algorithm for the staggered grid material point method. *Int J Mech Mater Des* 17(4):743–766. <https://doi.org/10.1007/s10999-021-09557-7>
- Khazaei C, Hazzard J, Chalaturnyk R (2015) Damage quantification of intact rocks using acoustic emission energies recorded during uniaxial compression test and discrete element modeling. *Comput Geotech* 67:94–102. <https://doi.org/10.1016/j.compgeo.2015.02.012>
- Kou MM, Liu XR, Wang ZQ, Tang SD (2021) Laboratory investigations on failure, energy and permeability evolution of fissured rock-like materials under seepage pressures. *Eng Fract Mech* 247:107694. <https://doi.org/10.1016/j.engfracmech.2021.107694>
- Lin QB, Cao P, Wen GP, Meng JJ, Cao RH, Zhao ZY (2021) Crack coalescence in rock-like specimens with two dissimilar layers and pre-existing double parallel joints under uniaxial compression. *Int J Rock Mech Min Sci* 139:104621. <https://doi.org/10.1016/j.ijrmmms.2021.104621>
- Liu L, Li H, Li X, Wu R (2020) Full-field strain evolution and characteristic stress levels of rocks containing a single pre-existing flaw under uniaxial compression. *Bull Eng Geol Environ*. <https://doi.org/10.1007/s10064-020-01764-4>
- Lu MK, Zhang HW, Zheng YG, Zhang L (2016) A multiscale finite element method with embedded strong discontinuity model for the simulation of cohesive cracks in solids. *Comput Method Appl Mech Eng* 311:576–598. <https://doi.org/10.1016/j.cma.2016.09.006>
- Nairn JA (2003) Material point method calculations with explicit cracks. *Comp Model Eng Sci* 4(6):649–664. <https://doi.org/10.3970/cmcs.2003.004.649>
- Omer M, Kareem A (2004) Fracture mechanisms of offset rock joints-A laboratory investigation. *Geotech Geol Eng* 22:545–562. <https://doi.org/10.1023/B:GEGE.0000047045.89857.06>
- Rezanezhad M, Lajevardi SA, Karimpouli S (2019) Effects of pore-crack relative location on crack propagation in porous media using XFEM method. *Theor Appl Fract Mec* 103:102241. <https://doi.org/10.1016/j.tafmec.2019.102241>
- Signetti S, Heine A (2021) Characterization of the transition regime between high-velocity and hypervelocity impact: thermal effects and energy partitioning in metals. *Int J Impact Eng* 151(2):103774. <https://doi.org/10.1016/j.ijimpeng.2020.103774>
- Sulsky D, Chen Z, Schreyer HL (1994) A particle method for history-dependent materials. *Comput Meth Appl Mech Eng* 118(1):179–196. [https://doi.org/10.1016/0045-7825\(94\)90112-0](https://doi.org/10.1016/0045-7825(94)90112-0)
- Vahab S, Hadi H, Mohammad F (2017) Fracture mechanism of brazilian discs with multiple parallel notches using PFC2D. *Period Polytech Civ Eng* 61(4):653–663. <https://doi.org/10.3311/PPci.10310>
- Vaucorbeil A, Nguyen VP, Hutchinson CR, Barnett MR (2022) Total Lagrangian material point method simulation of the scratching of high purity coppers. *Int J Solids Struct* 239–240:111432. <https://doi.org/10.1016/j.ijsolstr.2022.111432>

- Wang B, Karuppiiah V, Lu H, Komanduri R, Roy S (2005) Two-dimensional mixed mode crack simulation using the material point method. *Mech Adv Mater Struct* 12(6):471–484. <https://doi.org/10.1080/15376490500259293>
- Yang SQ, Jing HW (2011) Strength failure and crack coalescence behavior of brittle sandstone samples containing a single fissure under uniaxial compression. *Int J Fract* 168(2):227–250. <https://doi.org/10.1007/s10704-010-9576-4>
- Yang P, Yan L, Xiong Z, Xu Z, Zhao Y (2012) Simulation of fragmentation with material point method based on guron model and random failure. *Comput Model Eng Ences* 85(3):207–237. <https://doi.org/10.3970/cmcs.2012.085.207>
- Yang SK, Ma GW, Ren XH, Ren F (2014) Cover refinement of numerical manifold method for crack propagation simulation. *Eng Anal Bound Elem* 43:37–49. <https://doi.org/10.1016/j.enganabound.2014.03.005>
- Yang SK, Cao MS, Ren XH, Ma GW, Zhang JX, Wang HJ (2018) 3D crack propagation by the numerical manifold method. *Comput Struct* 194:116–129. <https://doi.org/10.1016/j.compstruc.2017.09.008>
- Yu SY, Ren XH, Zhang JX, Wang HJ, Sun ZH (2021) An improved form of smoothed particle hydrodynamics method for crack propagation simulation applied in rock mechanics. *Int J Min Sci Techno* 31(3):421–428. <https://doi.org/10.1016/j.ijmst.2021.01.009>
- Zhang DZ, Zou QS, VanderHeyden WB, Ma X (2008) Material point method applied to multiphase flows. *J Comput Phys* 227(6):3159–3173. <https://doi.org/10.1016/j.jcp.2007.11.021>
- Zhang X, Chen Z, Liu Y (2017) *The material point method*. Academic Press
- Zhang YN, Deng HW, Deng JR, Liu CJ, Yu ST (2020) Peridynamic simulation of crack propagation of non-homogeneous brittle rock-like materials. *Theor Appl Fract Mech* 106:102438. <https://doi.org/10.1016/j.tafmec.2019.102438>
- Zhao Y, Shen MX, Bi J, Wang CL, Yang YT, Du B, Ning L (2022) Experimental study on physical and mechanical characteristics of rock-concrete combined body under complex stress conditions. *Constr Build Mater* 324:126647. <https://doi.org/10.1016/j.conbuildmat.2022.126647>
- Zhou XP, Zhao Y, Qian QH (2015) A novel meshless numerical method for modeling progressive failure processes of slopes. *Eng Geol* 192:139–153. <https://doi.org/10.1016/j.enggeo.2015.04.005>

**Publisher's Note** Springer Nature remains neutral with regard to jurisdictional claims in published maps and institutional affiliations.

Springer Nature or its licensor (e.g. a society or other partner) holds exclusive rights to this article under a publishing agreement with the author(s) or other rightsholder(s); author self-archiving of the accepted manuscript version of this article is solely governed by the terms of such publishing agreement and applicable law.